

Received March 4, 2021, accepted March 15, 2021, date of publication March 17, 2021, date of current version March 30, 2021.

Digital Object Identifier 10.1109/ACCESS.2021.3066925

Multi-Objective Digital PID Controller Design in Parameter Space and Its Application to Automated Path Following

HAOAN WANG^{1,2}, (Member, IEEE), SUKRU YAREN GELBAL^{1,2},
AND LEVENT GUVENC^{1,2,3}, (Member, IEEE)

¹Automated Driving Laboratory, The Ohio State University, Columbus, OH 43212, USA

²Department of Electrical and Computer Engineering, The Ohio State University, Columbus, OH 43210, USA

³Department of Mechanical and Aerospace Engineering, The Ohio State University, Columbus, OH 43210, USA

Corresponding author: Levent Guvenc (guvenc.1@osu.edu)

ABSTRACT This paper presents a multi-objective digital PID controller design method using the parameter space approach of robust control. Absolute stability is treated first by finding the digital PID controller gain parameter space corresponding to closed loop poles being inside the unit circle. Additionally, phase margin, gain margin and a mixed sensitivity bound are treated as frequency domain constraints. Determination of digital PID controller parameter space regions satisfying these constraints is presented. All of these regions are superimposed to obtain a multi-objective digital PID controller gain parameter space solution region. The path following controller design of an automated driving vehicle is used as an example to illustrate the method. This multi-objective parameter space design approach can be extended to other digital controller forms also.

INDEX TERMS Digital PID control, parameter space methods, multi-objective control design.

I. INTRODUCTION

The parameter space approach is a part of the parametric approach to robust control [1]–[3]. Using the method of mapping frequency domain bounds to the chosen parameter space, the method can be applied to treat frequency domain uncertainty as well [2]–[4]. Traditionally, parameter space based control design methods have used continuous time representations even though current control implementations are digital. The parameter space approach is computationally fast, has the advantage of obtaining solution regions rather than one set of controller gains and can easily handle time delays but lacks from the need to pre-specify the controller structure and being able to handle only two parameters at a time [3], [5]. Parameter space robust control has recently been used successfully in a large number of applications ranging from yaw stability control and steering control to control of actuation in atomic force microscopy [6]–[10]. Several researchers have applied the parameter space approach to continuous time PID controllers for which the above-mentioned weaknesses of the parameter space approach are

overcome as the controller structure is fixed and as there are only three controller parameters to be tuned, i.e. the proportional, integral and derivative gains [11]–[13].

Although there is previous work on continuous time PID controller design in parameter space [3], [11], corresponding results are missing for digital PID controllers. While it is always possible to design a continuous time PID controller and then discretize it for a digital implementation, it is preferable to directly design the digital PID in the z-domain especially in the presence of a sampling time that is not too small which is typical for automotive control systems that rely on measurements from the CAN bus. This paper, therefore, focuses on a direct multi-objective digital PID design in the z-domain for absolute stability and for satisfying desired gain margin, phase margin and mixed sensitivity bound constraints.

Starting with the Ziegler-Nichols methods, PID control design has been traditionally based on tuning rules being empirically determined or derived for optimizing a time domain criterion for continuous time systems [14], [15]. First order or second order plant models with time delay are used in most of the PID controller design papers in the literature [15]. A continuous time first-order plus dead time (FOPDT) plant

The associate editor coordinating the review of this manuscript and approving it for publication was Chao-Yang Chen .

was treated in reference [16] for example. In reference [17], a continuous time second order plant with time delay was treated and a genetic algorithm was used for optimization based tuning. There are a lot of PID application papers where the PID design is introduced in the context of an important and demanding application. An example of such recent work is given in reference [18] where the PID design has focused on auto-tuning type adaptive PID systems applied to a wind turbine power regulation system treating a plant model with nonlinearity.

It should be noted that while most PID controller design and tuning methods presented in the literature are for continuous time designs, control systems including PID controllers are implemented digitally. PID controllers should, thus, be designed directly as digital controllers in order for their designed performance not to be degraded later due to the effect of sampling as very high sampling rates are usually not possible in most applications. It is for this reason that this paper focuses on the design of digital PID controllers instead of treating the easier to handle and well-established continuous time PIDs. While fewer in number, there have also been several papers in the literature that treat digital PID controller design. One recent example uses a genetic algorithm for optimizing digital PID gains for well known time domain criteria [19]. Just like similar approaches for continuous time PID controller design, a low order plant model with time delay is treated [19]. Most of the recent digital PID controller design papers are on application to a specific problem like CAN based dc motor control [20] and use an optimization method like particle swarms [20] or like a voltage source inverter application [21]. Digital PID controller design approaches that can treat general plants instead of low order fixed forms, that can handle multi-objective constraints, that offer ease of visualization to the designer through graphical representations of stability and performance regions rather than obtaining one possible solution within that PID controller parameter space through optimization are needed. This is the motivation for the current paper that proposes and presents a multi-objective parameter space solution approach for digital controller design.

It should be noted that there are also more advanced digital controllers formulated for switching type nonlinear plants. An example is reference [22] which is on sampled data adaptive fuzzy stabilization for a switched uncertain nonlinear system. In [22], stability is investigated using Lyapunov stability analysis. In contrast, this paper focuses on linear plants under digital PID control and does not treat switching nonlinear systems which are variable structure. This paper focuses on developing and using the parameter space approach for design and guarantees stability by keeping all poles inside the unit circle. The advantage and merit of using the proposed digital PID controller of this paper for plants that do not have too much uncertainty or switching behavior is that the design process is intuitive and very easy to automate, with a visual interpretation of a solution region of controller gains rather than one controller.

The contributions of this paper are: 1) analytical treatment of digital PID controller design, 2) using a multi-objective approach by calculating and superimposing stability constraints, phase margin bounds, gain margin bounds and mixed sensitivity bounds in the same controller parameter space, 3) not being constrained to plants that are first or second order with a delay and, instead, being able to treat plants of any order with time delay, 4) the ability to easily extend and apply the design approach to other fixed order controllers beyond PID controllers, if needed, 5) guaranteeing a stable design automatically by calculating the stable region of PID gains, 6) being able to easily incorporate the sampling time into the computation process to evaluate its effect on the solution region obtained.

The rest of paper is organized as follows. Section II presents the parameter space approach based robust PID controller design in the z -domain, where absolute stability, phase margin constraint, gain margin constraint and mixed sensitivity constraint are considered. In Section III, an example is used for illustrating multi-objective z -domain robust PD control satisfying phase margin and mixed sensitivity bound constraints simultaneously, using a vehicle model with validated parameters. In Section IV, designed robust digital PD controller is applied to the autonomous vehicle path following control system in a simulation analysis, with different types of paths, parameter perturbations and sensor noise. The paper ends with conclusions in Section V.

II. PARAMETER SPACE APPROACH IN Z-DOMAIN

A. ABSOLUTE STABILITY IN THE Z DOMAIN

Let the characteristic equation of a feedback control system with control gains k and uncertain parameters q be given by $p(s, q, k) = 0$ in the s domain. Hurwitz stability requires all roots of the characteristic equation $p(s, q, k) = 0$, to lie in the left-half plane. The parameter space solution is based on the Boundary Crossing Theorem which states that characteristic equation roots need to cross the stability boundary to go from stable to unstable ones and vice versa as parameters are changed [2]. The continuous time stability boundary can be crossed through the real root boundary (RRB), complex root boundary (CRB) or infinite root boundary (IRB) [2].

The corresponding absolute stability region in the z -domain is the inside of the unit circle. The Boundary Crossing Theorem is applicable again and transitions of characteristic equation roots from inside the unit circle (stable) to the outside of the unit circle (unstable) are only possible by crossing the unit circle as parameters are varied. In the z -domain there is only the complex root boundary CRB around the unit circle and the real root boundaries RRB at $z = 1$ and $z = -1$. An infinite root boundary IRB does not exist for z -domain absolute stability.

The unit circle is given by

$$z = e^{sT} = e^{j\omega T} = e^{j\theta} = \cos \theta + j \sin \theta \quad (1)$$

where $\theta \equiv \omega T \in [0, 2\pi]$ and T is the sampling time. Consider the standard digital PID controller given by

$$C(z, k) = k_p + k_i \frac{z}{z-1} + k_d \frac{z-1}{z} \quad (2)$$

where k_p, k_i and k_d (altogether the control gains k) are the proportional, integral and derivative gains, respectively. In a generic digital feedback control system with controller $C(z, k)$ and plant $G(z, q)$ with q representing the parametric plant uncertainty, the loop gain is the product of all transfer functions in the loop as

$$L(z) = C(z)G(z) \quad (3)$$

where k and q are not used in C and G for the sake of brevity. The closed loop transfer function is:

$$G_{cl}(z) = \frac{C(z)G(z)}{1 + C(z)G(z)} \quad (4)$$

The characteristic equation can be derived as

$$p(z, k, q) \equiv 1 + C(z)G(z) = 0 \quad (5)$$

Substitute (2) into (5) to obtain

$$(z-1)z + G(z) \left(k_p(z-1)z + k_i z^2 + k_d(z-1)^2 \right) = 0 \quad (6)$$

as the characteristic equation of the digital PID controlled plant.

The complex root boundary CRB will be computed using (6). Substitute the unit circle boundary $z = e^{j\theta} = \cos \theta + j \sin \theta$ and $G(z) = \text{Re}_G + j \text{Im}_G$ into (6) and separate the real part denoted by Re and the imaginary part denoted by Im of (6) to obtain the following two equations which can be used for calculating two free PID design parameters.

$$\begin{aligned} \text{Real : } & (1 + K_{pid} \text{Re}_G) \cos 2\theta - K_{pid} \text{Im}_G \sin 2\theta \\ & - (1 + K_{p2d} \text{Re}_G) \cos \theta + K_{p2d} \text{Im}_G \sin \theta + \text{Re}_G k_d = 0 \end{aligned} \quad (7)$$

$$\begin{aligned} & (1 + K_{pid} \text{Re}_G) \sin 2\theta + K_{pid} \text{Im}_G \cos 2\theta \\ & - (1 + K_{p2d} \text{Re}_G) \sin \theta - K_{p2d} \text{Im}_G \cos \theta + \text{Im}_G k_d = 0 \end{aligned} \quad (8)$$

where

$$K_{pid} \equiv k_p + k_i + k_d \quad (9)$$

$$K_{p2d} \equiv k_p + 2k_d. \quad (10)$$

A sweep of angle $\theta \in (0, 2\pi)$ is used to solve (7) and (8) above for any two of the three digital PID controller gains. When one of the digital PID gains is zero in the case of PI or PD controllers, (7) and (8) provide the solution region in the corresponding controller parameter space. When all three digital PID gains are present, it is possible to solve (7) and (8) for a grid of possible values of one of the control parameters and to obtain a three-dimensional absolute stability solution region.

The real root boundary RRB is calculated using $z = 1(\theta = 0^\circ)$ and $z = -1(\theta = 180^\circ)$ in (7) and (8) above

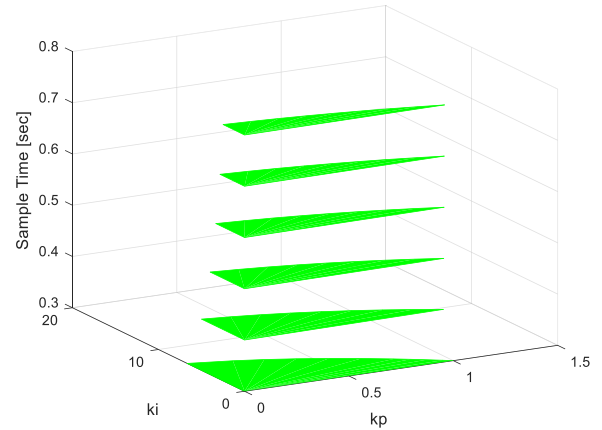


FIGURE 1. Digital PI controller gains $k_p - k_i$ solution region scheduled by sample time T . The green colored controller gains region is largest for the smaller sampling time and decreases in size as the sample time is increased.

or (6). Note that these equations will degenerate into a single equation for each of the two real root boundaries. For the real root boundary at $z = 1$, the RRB equation is $k_i = 0$. The RRB at $z = -1$ corresponds to a singular solution and the RRB equation is

$$2k_p + 4k_d + k_i = -\frac{1}{G(z)|_{z=-1}} \quad (11)$$

(7) and (8) can be combined into the matrix equation

$$Ak \equiv \begin{bmatrix} a_{11} & a_{12} & a_{13} \\ a_{21} & a_{22} & a_{23} \end{bmatrix} \begin{bmatrix} k_p \\ k_i \\ k_d \end{bmatrix} = \begin{bmatrix} b_1 \\ b_2 \end{bmatrix} \equiv b \quad (12)$$

where

$$\begin{aligned} a_{11} &= \text{Re}_G \cos 2\theta - \text{Im}_G (\sin 2\theta + \cos \theta + \sin \theta) \\ a_{12} &= \text{Re}_G (\cos 2\theta + 1) - \text{Im}_G (\sin 2\theta + 2 \cos \theta + 2 \sin \theta) \\ a_{13} &= \text{Re}_G (\cos 2\theta + 1) - \text{Im}_G (\sin 2\theta + 2 \cos \theta + 2 \sin \theta) \\ a_{21} &= \text{Re}_G (\sin 2\theta + \sin \theta) + \text{Im}_G (\cos 2\theta - \cos \theta) \\ a_{22} &= \text{Re}_G (\sin 2\theta + 2 \sin \theta) + \text{Im}_G (\cos 2\theta - 2 \cos \theta + 1) \\ a_{23} &= \text{Re}_G \sin 2\theta + \text{Im}_G \cos 2\theta \\ b_1 &= -\cos(2\theta) + \cos(\theta) \\ b_2 &= -\sin(2\theta) + \sin(\theta) \end{aligned}$$

Frequencies $\theta = \omega T$ that make $\text{rank}(A) = \text{rank}([A : b]) = 1$ (or $b \in \text{range}(A)$) are singular frequencies and result in infinitely many solutions corresponding to a line in the chosen space of two controller parameters.

As an example, consider the plant $G(z) = \frac{1}{z(z+1)}$ for PD and PI controller design. Fig. 1 and Fig. 3 illustrate 3D plots where (k_p, k_i) and (k_d, k_p) are scheduled by sampling time $T \in [0.3, 0.8]$ sec on the third, vertical axis. Fig. 2 and Fig. 4 show detailed views of k_p, k_i and k_d, k_p parameter spaces and pole locations within the z -plane when sample time is 0.3 sec. The shaded blue area represents the stable region and it can be seen that when $(k_p, k_i)(k_d, k_p)$ points are selected inside the stable region, on the stable boundary and outside

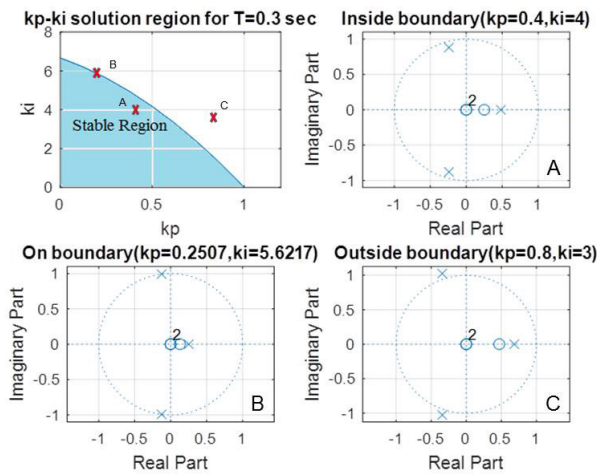


FIGURE 2. Digital PI controller parameter plane at top left. The points marked with X and labeled A, B and C correspond to gains for stable, marginally stable and unstable pole locations. Top right plot shows poles for gains A which are all inside the unit circle for a stable design. Bottom left plot shows poles for gains B and has two poles on the unit circle for a marginally stable design. This corresponds to boundary crossing of the unit circle complex root boundary. Bottom right plot shows poles for gains C two of which are outside the unit circle for an unstable design.

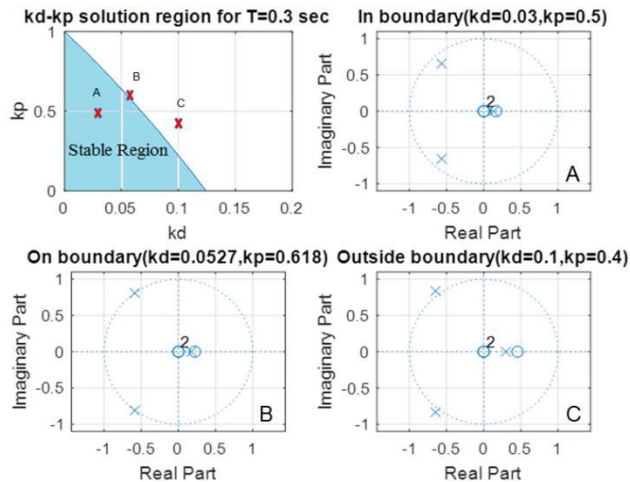


FIGURE 4. Digital PD controller parameter plane at top left. The points marked with X and labeled A, B and C correspond to gains for stable, marginally stable and unstable pole locations. Top right plot shows poles for gains A which are all inside the unit circle for a stable design. Bottom left plot shows poles for gains B and has two poles on the unit circle for a marginally stable design. This corresponds to boundary crossing of the unit circle complex root boundary. Bottom right plot shows poles for gains C two of which are outside the unit circle for an unstable design.

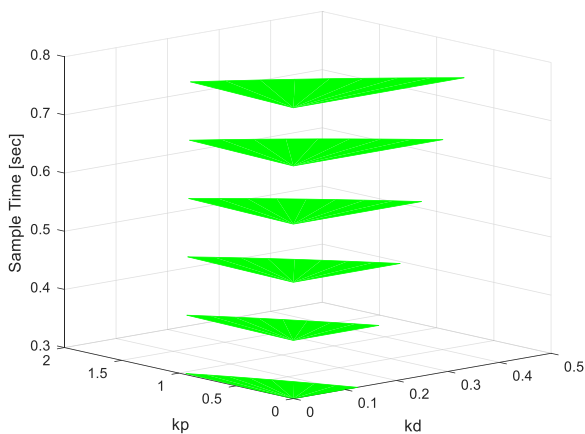


FIGURE 3. Digital PD controller gains $k_p - k_d$ solution region scheduled by sample time T . The green colored controller gains region is smallest for the smaller sampling time and increases in size as the sample time is increased.

the stable region, the corresponding two poles of the closed loop transfer function (4) are inside the unit circle, on the unit circle and outside the unit circle, respectively, as expected.

B. PHASE MARGIN CONSTRAINT IN THE Z-DOMAIN

From (1), we get the following equation:

$$z = e^{sT} = e^{j\omega T} = \cos \omega T + j \sin \omega T \tag{13}$$

Consider ω_{gc} as the gain crossover frequency where the loop gain $L(z)$ is unity or zero decibels as

$$|L(z)| = \left| L \left(e^{j\omega_{gc} T} \right) \right| = 1 \tag{14}$$

The expression of the phase margin PM is

$$L(z) = e^{j(PM - \pi)} = -\cos(PM) - j \sin(PM) \tag{15}$$

Substituting from (3) into (15), the real and imaginary component equations of $L(z)$ are written as

$$\text{Re}(L(z)) = \text{Re}(C(z)G(z)) = -\cos(PM) \tag{16}$$

$$\text{Im}(L(z)) = \text{Im}(C(z)G(z)) = -\sin(PM) \tag{17}$$

Substituting (2) into (16), (17), we obtain

$$\text{Re} \left(\left(k_p + k_i \frac{z}{z-1} + k_d \frac{z-1}{z} \right) G(z) \right) = -\cos(PM) \tag{18}$$

$$\text{Im} \left(\left(k_p + k_i \frac{z}{z-1} + k_d \frac{z-1}{z} \right) G(z) \right) = -\sin(PM) \tag{19}$$

where the PID control gains in (18) and (19) can be expressed as follows:

$$\begin{aligned} \left(k_p + k_i \frac{z}{z-1} + k_d \frac{z-1}{z} \right) \Big|_{z=\cos \theta + j \sin \theta} &= \\ &= k_p + k_i \frac{(\cos \theta + j \sin \theta)}{(\cos \theta + j \sin \theta) - 1} + k_d \frac{(\cos \theta + j \sin \theta) - 1}{(\cos \theta + j \sin \theta)} \\ &= k_p + k_i \frac{(\cos \theta + j \sin \theta)((\cos \theta - 1) - j \sin \theta)}{((\cos \theta - 1) + j \sin \theta)((\cos \theta - 1) - j \sin \theta)} \\ &\quad + k_d \frac{(\cos \theta + j \sin \theta - 1)(\cos \theta - j \sin \theta)}{(\cos \theta + j \sin \theta)(\cos \theta - j \sin \theta)} \\ &= k_p + k_i \frac{1 - \cos \theta - j \sin \theta}{(\cos \theta - 1)^2 + (\sin \theta)^2} + k_d (1 - \cos \theta + j \sin \theta) \end{aligned} \tag{20}$$

Substituting (20) and $G(z) = \text{Re}_G + j \text{Im}_G$ into (18) and (19), (21) and (22) are derived for solving the parameters of the PID controller which satisfy the phase margin constraint as

$$\begin{aligned} k_p \text{Re}_G + \frac{k_i (\text{Re}_G (1 - \cos \theta) + \text{Im}_G \sin \theta)}{2(1 - \cos \theta)} \\ + k_d (\text{Re}_G (1 - \cos \theta) - \text{Im}_G \sin \theta) = -\cos(PM) \end{aligned} \tag{21}$$

$$k_p \text{Im}_G + \frac{k_i (\text{Im}_G(1 - \cos \theta) - \text{Re}_G \sin \theta)}{2(1 - \cos \theta)} + k_d (\text{Re}_G \sin \theta + \text{Im}_G(1 - \cos \theta)) = -\sin(PM) \quad (22)$$

Using a grid of $\theta \in (0, 2\pi)$, (21) and (22) can be used to obtain the parameter space region in any two of the digital PID gains when the other one is fixed. Boundedness of the solution as in reference [18] requires the denominator term $(1 - \cos \theta)$ in (21) and (22) not to go to zero which means that θ should not become zero. That is why zero is avoided in the grid $\theta \in (0, 2\pi)$.

C. GAIN MARGIN CONSTRAINT VIA Z-PLANE

Consider the phase crossover frequency ω_{gc} where the phase becomes -180° given by

$$\angle L(z) = \angle L(e^{j\omega_{gc}T}) = -180^\circ \quad (23)$$

$$L(z) = L(e^{j\omega_{gc}T}) = \frac{1}{M} \angle -180^\circ = -\frac{1}{M} \quad (24)$$

where $M = 10^{(\frac{GM}{20})}$ and GM is gain margin bound in decibels (dB). Substituting (3) into (24), the real and imaginary component equations of $L(z)$ are written as

$$\text{Re}(L(z)) = \text{Re}(C(z)G(z)) = -\frac{1}{M} \quad (25)$$

$$\text{Im}(L(z)) = \text{Im}(C(z)G(z)) = 0 \quad (26)$$

Substituting (2) into (25) and (26), we obtain:

$$\text{Re} \left((k_p + k_i \frac{z}{z-1} + k_d \frac{z-1}{z}) G(z) \right) = -\frac{1}{M} \quad (27)$$

$$\text{Im} \left((k_p + k_i \frac{z}{z-1} + k_d \frac{z-1}{z}) G(z) \right) = 0 \quad (28)$$

Substituting (20) and $G(z) = \text{Re}_G + j\text{Im}_G$ into (27) and (28), (29) and (30) are derived as

$$k_p \text{Re}_G + \frac{k_i (\text{Re}_G(1 - \cos \theta) + \text{Im}_G \sin \theta)}{2(1 - \cos \theta)} + k_d (\text{Re}_G(1 - \cos \theta) - \text{Im}_G \sin \theta) = -\frac{1}{M} \quad (29)$$

$$k_p \text{Im}_G + \frac{k_i (\text{Im}_G(1 - \cos \theta) - \text{Re}_G \sin \theta)}{2(1 - \cos \theta)} + k_d (\text{Re}_G \sin \theta + \text{Im}_G(1 - \cos \theta)) = 0 \quad (30)$$

and can be used for solving two parameters of the digital PID controller which satisfy the gain margin constraint. Boundedness of the solution as in reference [18] requires the denominator term $(1 - \cos \theta)$ in (29) and (30) not to go to zero which means that θ should not become zero. This will be achieved by using a grid in $\theta \in (0, 2\pi)$ which avoids zero frequency.

D. MIXED SENSITIVITY CONSTRAINT IN THE Z-DOMAIN

Mixed sensitivity design aims to map frequency domain criteria of robust control into parameter space, which must satisfy the following robust performance requirement

$$\| |W_S S| + |W_T T| \|_\infty < 1 \text{ or } |W_S S| + |W_T T| < 1, \quad \forall \omega \quad (31)$$

where $\forall \omega$ means for all values of frequency ω , $S = 1/(1+L)$ and $T = L/(1+L)$ are sensitivity and complementary sensitivity functions W_S and W_T are corresponding weights. Different choices of weight functions $W_S(s)$ and $W_T(s)$ in the s domain were introduced in [3]. Similar first order discrete time weight transfer functions $W_S(z)$ and $W_T(z)$ can be derived using the zero-order hold method from these or they can be designed directly in discrete time.

The mixed sensitivity constraint can be expressed as

$$|W_S(z)| + |W_T(z)L(z)| = |1 + L(z)| \quad (32)$$

$$L(z) = |L(z)| \angle \theta_L = |L(z)| e^{j\theta_L} \quad (33)$$

where the solution of $|L(z)|$ can be expressed as:

$$|L(z)| = \frac{-\cos \theta_L + |W_S(z)| |W_T(z)| \pm \sqrt{\Delta}}{1 - |W_T(z)|^2} \quad (34)$$

where

$$\Delta = \cos^2 \theta_L + |W_S(z)|^2 + |W_T(z)|^2 - 2 |W_S(z)| |W_T(z)| \cos \theta_L - 1, \quad \theta_L \in [0, 2\pi], \Delta \geq 0 \quad (35)$$

$L(z)$ can be presented in terms of a controller K as shown in the equation:

$$L(z) = K(z)G(z) = (K_R + jK_I)G(z) \quad (36)$$

which can be used to solve for the real part K_R and imaginary part K_I of the controller. Based on the PID controller expression, (37) is derived as:

$$K_R + jK_I = k_p + k_i \frac{z}{z-1} + k_d \frac{z-1}{z} \quad (37)$$

Separating the real and imaginary parts of (36) and substituting into (37), the following (38) are derived

$$\begin{cases} K_R = k_p + k_i \frac{1 - \cos \theta}{(\cos \theta - 1)^2 + (\sin \theta)^2} + k_d(1 - \cos \theta) \\ K_R = k_p + \frac{k_i}{2} + k_d(1 - \cos \theta) \\ K_I = -k_i \frac{\sin \theta}{(\cos \theta - 1)^2 + (\sin \theta)^2} + k_d \sin \theta \\ K_I = -k_i \frac{\sin \theta}{2(1 - \cos \theta)} + k_d \sin \theta \end{cases} \quad (38)$$

Note that K_R and K_I given above in (38) are variable with θ . The PID controller gains are solved using these equations and also depend on θ . This will require a boundedness analysis on the PID gains. A boundedness analysis was also used in reference [18] for their PID controller. It should be noted that the PID controlled system of this paper is guaranteed to be stable by design as its poles are constrained to lie within the unit circle. In the boundedness analysis, it is first noted from (38) that K_R will never blow up while K_I can go to infinity only as $\theta \rightarrow 0$. So, the grid based solution uses $\theta \in (0, 2\pi)$ which avoids zero frequency.

For PD controller parameters k_d and k_p (38) become

$$k_d = \frac{K_I}{\sin \theta} \quad (39)$$

$$k_p = K_R - k_d(1 - \cos \theta) = K_R - K_I \frac{(1 - \cos \theta)}{\sin \theta} \quad (40)$$

For PI controller parameters k_p and k_i , (38) become

$$k_i = -\frac{K_I ((\cos \theta - 1)^2 + (\sin \theta)^2)}{\sin \theta} = -K_I \frac{2(1 - \cos \theta)}{\sin \theta} \quad (41)$$

$$k_p = K_R - k_i \frac{1 - \cos \theta}{(\cos \theta - 1)^2 + (\sin \theta)^2} = K_R + \frac{K_I(1 - \cos \theta)}{\sin \theta} \quad (42)$$

When θ is not allowed to be zero, the PD and PI gains in (39)-(42) are all bounded. For PID controller design, substituting from (38) into (36), using $G(z) = \text{Re}_G + j\text{Im}_G$ and separating the real and imaginary parts, (43) and (44) are derived

$$k_p \text{Re}_G + \frac{k_i (\text{Re}_G(1 - \cos \theta) + \text{Im}_G \sin \theta)}{(\cos \theta - 1)^2 + (\sin \theta)^2} + k_d (\text{Re}_G(1 - \cos \theta) - \text{Im}_G \sin \theta) = |L(z)| \cos \theta_L \quad (43)$$

$$k_p \text{Im}_G + \frac{k_i (\text{Im}_G(1 - \cos \theta) - \text{Re}_G \sin \theta)}{(\cos \theta - 1)^2 + (\sin \theta)^2} + k_d (\text{Re}_G \sin \theta + \text{Im}_G(1 - \cos \theta)) = |L(z)| \sin \theta_L \quad (44)$$

The equations presented in this section can be used to determine the PID controller gain parameter space regions where absolute stability, gain margin, phase margin and mixed sensitivity bounds are satisfied. This is illustrated with an example in the next section.

The algorithms that will be used to implement the proposed parameter space multi-objective digital PID controller design scheme in practice is presented in the following algorithm.

The design parameters used in this paper are the desired minimum phase margin PM , the desired minimum gain margin M and the weights W_S and W_T of the mixed sensitivity bound. The desired phase margin PM should be about 70° or more for a good nominal design and between 45° to 60° would be good values for a robust design considering uncertainty in the plant being controlled. The desired gain margin M should be selected to be at least 2. These choices will result in a design with good damping properties and with some inherent robustness. W_S is chosen as a high pass filter, filtering low frequencies while W_T is chosen as a low pass filter. The bandwidth of W_S is chosen to correspond to be close to the actuator bandwidth of the controlled system. The bandwidth of W_T is chosen as the frequency at which significant uncertainty in our plant model starts in the form of unmodeled higher frequency dynamics. Low gains at low frequencies for W_S will improve disturbance rejection and reference command following. Low gain at high frequencies of W_T will stop the controlled system from responding at frequencies of high model uncertainty.

how to choose the design parameters in this paper and how these parameters influence the system performance

Algorithm 1 Design Algorithm of the Controller

Stability region

Step S1: Choose a grid of frequencies $\theta \in (0, \pi]$ where $\theta \equiv \omega T$ is the non-dimensional frequency.

Step S2: For each value of θ , solve (7) and (8) to find K_{pid} and K_{p2d} .

Step S3: Choose two out of the three PID gains k_p , k_i , k_d and solve (9) and (10) for those two.

Step S4: Plot the solution in the plane of the two PID gains chosen in Step S3.

Step S5: Check points inside regions in resulting controller parameter plane for stability (poles inside unit circle). Stable points mean the whole region is stable.

Phase margin bound region

Step PM1: Select a desired value of phase margin PM .

Step PM2: Choose a grid of frequencies $\theta \in (0, \pi]$.

Step PM3: For each value of θ , solve (21) and (22) to determine the two PID controller gains selected in Step S3 above.

Step PM4: Plot the solution in the plane of the two PID gains chosen in Step S3.

Step PM5: Check points to each side of lines in the resulting controller parameter plane for the phase margin and select region with phase margin larger than PM .

Gain margin bound region

Step GM1: Select a desired value of gain margin M .

Step GM2: Choose a grid of frequencies $\theta \in (0, \pi]$.

Step GM3: For each value of θ , solve (29) and (30) to determine the two PID controller gains selected in Step S3 above.

Step GM4: Plot the solution in the plane of the two PID gains chosen in Step S3.

Step GM5: Check points to each side of lines in the resulting controller parameter plane for the gain margin and select region with gain margin larger than M .

Mixed sensitivity bound region

Step MS1: Select desired sensitivity and complementary sensitivity weights W_S and W_T .

Step MS2: Choose a grid of frequencies $\theta \in (0, \pi]$.

Step MS3: For each value of θ execute main loop below.

Step MS4: Use a grid of angles $\theta_L \in [0, 2\pi]$.

Step MS5: For each value of θ_L , solve (34) and (35) for $|L|$.

Step MS6: Solve (36) for K_R and K_I .

Step MS7: Solve (38) to determine the two PID controller gains selected in Step S3 above.

Step MS8: Plot the solution in the plane of the two PID gains chosen in Step S3.

Step MS9: End loop on θ_L .

Step MS10: End loop on θ .

Step MS11: Check points inside regions in resulting controller parameter plane for satisfaction of the mixed sensitivity condition (31) and mark region as solution if satisfied.

Multi-objective solution region

Step MO1: Superimpose the stability, phase margin bound, gain margin bound and mixed sensitivity bound solution regions in the plane of the two PID gains chosen in Step S3. The region(s) that satisfy all of these constraints is the overall solution region.

Step MO2: If desired, change the value of the PID gain not selected and repeat whole procedure. Plot the solution region in the three dimensional PID controller gain parameter space.

Step MO3: Repeat Step MO2 until a three dimensional display of the PID gains solution space is obtained.



FIGURE 5. Ford Fusion automated experimental vehicle of the Automated Driving Lab at the Ohio State University. This drive-by-wire vehicle is equipped with sensors as well as data processing and control units to achieve autonomous driving. Its model parameters were validated through vehicle dynamics testing, to represent the vehicle inside the simulations with high accuracy and design realistic controllers.

III. MULTI-OBJECTIVE DIGITAL PD CONTROLLER DESIGN

A. THE VEHICLE AND PARAMETERS

In this section, the method presented in the previous section is applied to multi-objective design of a PD controller for the path following functionality of an automated driving vehicle, using the single track model described in [23] as the base model. This single track linear vehicle model uses numerical parameter values corresponding to the validated model of our Ford Fusion experimental vehicle shown in Fig. 5.

Parameters for the vehicle are given in Table 1. In the following parts of this section, these parameters were used for generating the transfer function $G(s)$ that was used to design the steering controller for automated path following.

B. CONTROLLER DESIGN

Consider the experimentally validated continuous time transfer function $G(s)$ of the Ford Fusion experimental vehicle model [23] of the Automated Driving Lab of the Ohio State University from the front wheel steering angle δ_f to lateral deviation from the desired path at the lookahead distance y given by

$$G(s) = \frac{y}{\delta_f} = \frac{227.6s^2 + 5536s + 36260}{s^2(s^2 + 22.16s + 37.92)} \quad (45)$$

$G(z)$ is discretized from $G(s)$ using the zero-order hold method with sampling time $T = 0.01$ as

$$G(z) = \frac{0.01147z^3 - 0.008747z^2 - 0.01145z + 0.009058}{z^4 - 3.798z^3 + 5.397z^2 - 3.4z + 0.8012} \quad (46)$$

A digital PD controller design is used here as the vehicle model in (45) is Type 2 and will achieve zero steady state error without the need to have integral action in the controller. The phase margin constraint and mixed sensitivity constraint objectives are taken into account simultaneously in the multi-objective digital PD controller design. The phase margin is required to be within $PM \in [20^\circ, 80^\circ]$ and the parameters for the mixed sensitivity constraint are: low frequency bound $l_s = 0.5$, high frequency bound $h_s = 4$ and approximate

TABLE 1. Vehicle parameters.

Mass (m)	2000 kg
Moment of Inertia (J)	3728 kgm ²
Front Axle Length (l_f)	1.30 m
Rear Axle Length (l_r)	1.55 m
Front Tire Cornering Coefficient (C_f)	1.9x10 ⁵ N/rad
Rear Tire Cornering Coefficient (C_r)	5x10 ⁵ N/rad
Lookahead Distance (l_s)	2 m

bandwidth $\omega_s = 5rad/s$ for sensitivity weight function W_S ; low frequency gain $l_T = 0.2$, high frequency gain $h_T = 1.8$ and the frequency of transition to significant model uncertainty $\omega_T = 120rad/s$ for complementary sensitivity weight function W_T . The weights used are given by:

$$(W_S(s))^{-1} = h_s \frac{s + \omega_s l_s}{s + \omega_s h_s} = 4 \frac{s + 2.5}{s + 20} \quad (47)$$

$$W_T(s) = h_T \frac{s + \omega_T l_T}{s + \omega_T h_T} = 1.8 \frac{s + 24}{s + 216} \quad (48)$$

Fig. 6 shows the $k_d - k_p$ solution region obtained for this multi-objective design and (k_d, k_p) are selected as (0.07, 0.2). It can be seen from Fig. 7 and Fig. 8 that the corresponding frequency responses satisfy the phase margin constraint, and the mixed sensitivity constraint is also satisfied with the chosen controller parameters as the magnitude plot is below the 0 dB ($(|W_S S| + |W_T T|) = 1$) line.

IV. SIMULATION TESTING AND EVALUATION

The designed digital PD feedback controller where $k_d = 0.07$, $k_p = 0.02$ and $T = 0.01$ sec is evaluated in autonomous vehicle path following simulations in this section. For the first subsection, several different paths were created for the vehicle to follow with relatively high speeds to test the path following performance. The simulation results of vehicle trajectory and vehicle lateral deviation error with the designed digital PD controller were displayed for each simulation and results were discussed. For the second subsection, simulations with parameter perturbations, disturbance and sensor noise were added to test the robustness of the controller.

A. PATH FOLLOWING SIMULATIONS

The first desired path to test the performance is an elliptical route where the vehicle drives at 60km/h and follows the path. Path following results were shown in the figures below. Fig. 9 shows the vehicle path with respect to the generated desired path and Fig. 10 shows lateral error, which indicates the tracking performance.

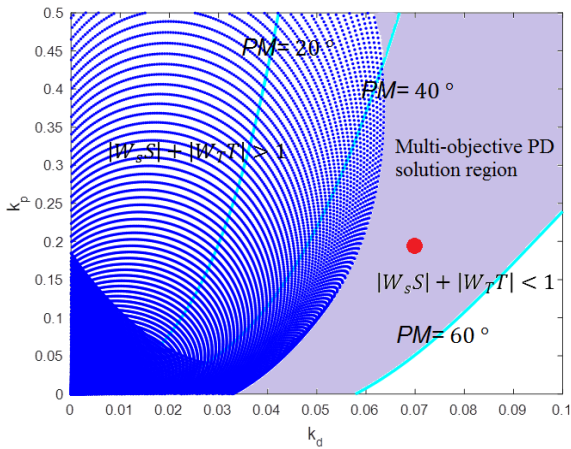


FIGURE 6. Multi-objective design graphical superposition diagram in PD controller parameter plane. Blue line area is where PD controller gains result in mixed sensitivity being larger than unity while the area outside its boundary is where PD controller gains satisfy the mixed sensitivity constraint. Note that mixed sensitivity can also be evaluated for $|W_s S| + |W_t T| < \gamma$ where $0 < \gamma < 1$. PD controller gain combination lines where the phase margin is 20°, 40° and 60° are also shown. The red dot shows the chosen design point where mixed sensitivity is satisfied and the phase margin is between 40° and 60°.

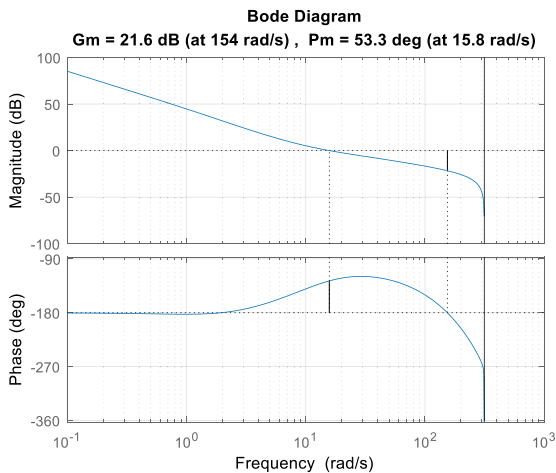


FIGURE 7. The phase margin achieved by the design (PD gains corresponding to red dot in Figure 6) is shown in these Bode plots. The phase margin for this design is 53.3° and margin is between 40° and 60° as desired.

As it can be seen from the figures above, the first path was followed by the vehicle easily with very small amount of error around curved road parts, at relatively high speed. The RMS value for the error is calculated as 0.0033m. The second desired path used in the simulation evaluation was selected to be a race track, which was aimed to be more challenging for the vehicle. The speed was set to 60km/h. The results are shown in the following figures, where Fig. 11 shows the desired path versus the vehicle path, and Fig. 12 shows the lateral error, in a similar fashion to the previous test results.

Although it was more challenging and resulted slightly larger error as compared to the previous one, the second path was also followed by the vehicle with very small amount of error. The RMS value for the error is calculated as 0.0134m.

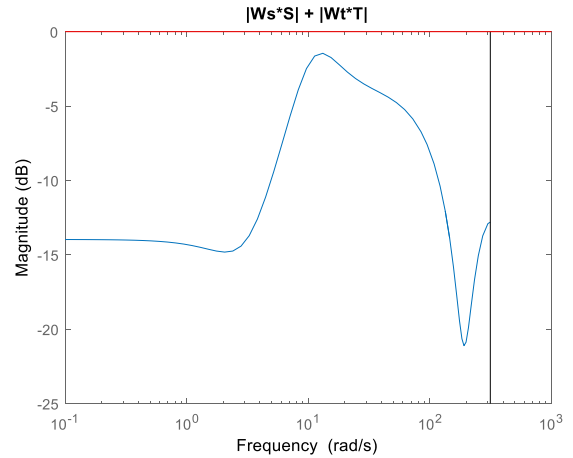


FIGURE 8. The mixed sensitivity magnitude $|W_s S| + |W_t T|$ is shown here for the digital PD controller designed. It is seen that the mixed sensitivity magnitude is less than unity at all frequencies as desired.

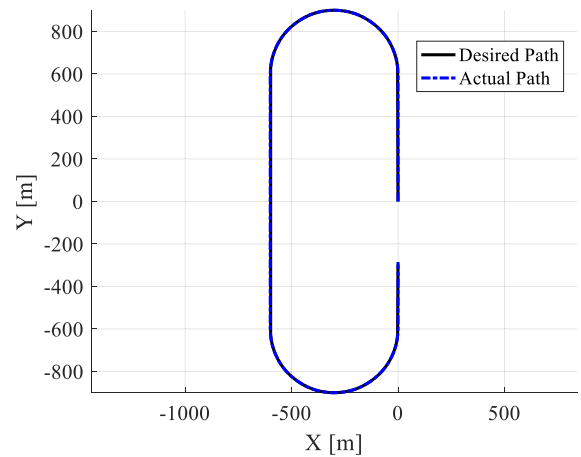


FIGURE 9. The automated path following vehicle's actual path and first desired path are superimposed in this figure. The vehicle is following an oval shaped path and the desired and actual paths are almost on top of each other.

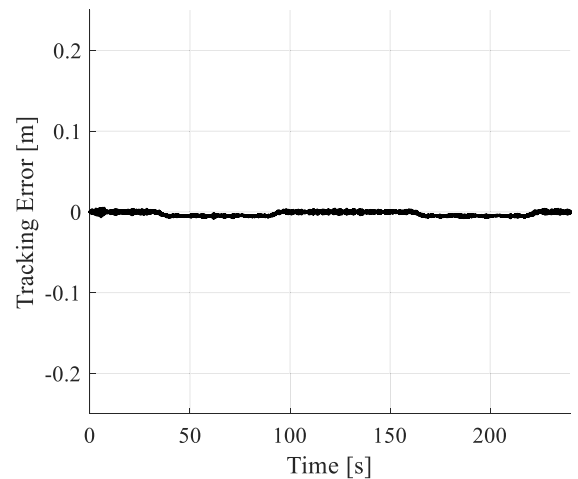


FIGURE 10. The automated path following vehicle's path tracking error is shown here while following the oval shaped desired path in Figure 8. The error values are very small showing that the parameter space designed multi-objective digital PD steering controller has performed satisfactorily.

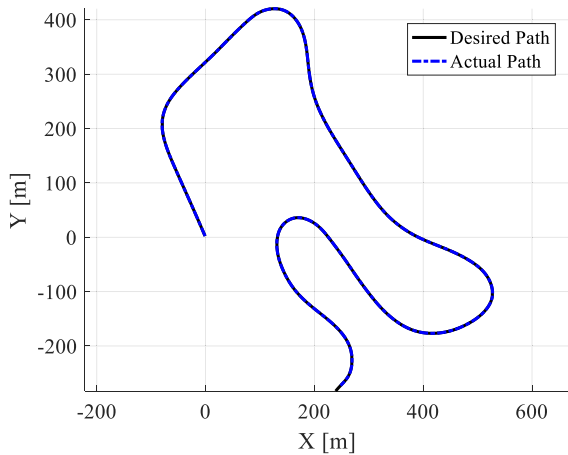


FIGURE 11. The automated path following vehicle’s actual path and second desired path are superimposed in this figure. The vehicle is following a race track shaped path and the desired and actual paths are almost on top of each other.

The third and final desired path was selected from a realistic environment from the Ohio State University’s Columbus campus, where the vehicle would possibly carry passengers. The path was generated using the route between the Scott Laboratory and Wexner Medical Center buildings. Speed was also set to a lower speed, 30mph because of the driving environment. Test results are shown in the following figures where Fig. 13 shows the desired path versus the vehicle path, and Fig. 14 shows the lateral error.

Even with sharper turns and the speed intentionally selected high for a campus environment, the vehicle still performs well. Error increases a lot during the sharp corners in the path as can be seen from Fig. 14, but it still stays below 0.5m all the time, and below 0.25m for most of the time. Therefore, the RMS value calculated for the error is actually very small, 0.0305m. The actual path that resulted from the simulation evaluation was also projected on top of the satellite image of the simulation site in order to represent the corresponding roads more realistically. The top-down view of this campus environment and the path represented by red line can be seen in Fig. 15 below.

By looking at the results, it is seen that the actual path and desired path almost overlap in all cases. RMS values for the error in all three cases are displayed in Table 2 as a summary of the evaluation. These values are also very small. Therefore, it can be seen that the vehicle performed well on all three different types of paths in the simulation environment, using the designed controller. The actual path deviation errors are expected to be at least an order of magnitude higher in a real implementation of this steering controller for path tracking due to the neglected model uncertainties, road surface conditions and disturbances that were not treated in the ideal model used here.

B. ROBUSTNESS SIMULATIONS

In this subsection, performance of the controller against parameter perturbations, disturbance and sensor noise will

TABLE 2. RMS values for lateral error in simulations.

Oval Path at 60km / h	Race Track at 60km / h	Campus Route at 30mph
0.0033m	0.0134m	0.0305m

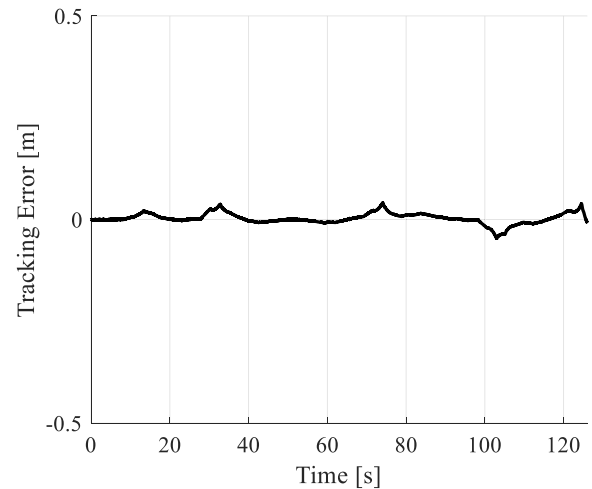


FIGURE 12. The automated path following vehicle’s path tracking error is shown here while following the race track shaped desired path of Figure 10. The error values are very small showing that the parameter space designed multi-objective digital PD steering controller has performed satisfactorily.

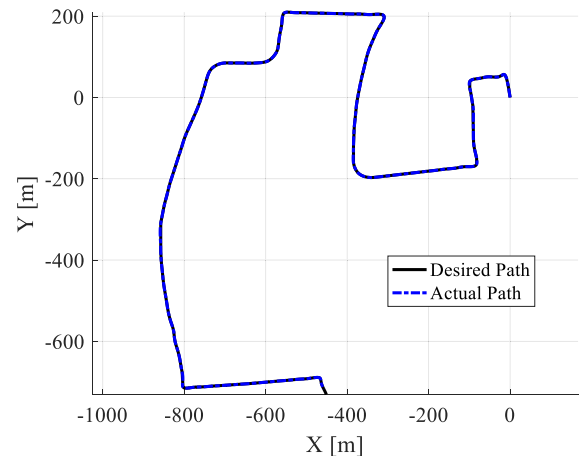


FIGURE 13. The automated path following vehicle’s actual path and third desired path are superimposed in this figure. The vehicle is following a path from the Ohio State University campus environment and the desired and actual paths are almost on top of each other.

be demonstrated. For this purpose, within the paths used in previous subsection for path following, the second path was selected. This race track path will be used for testing the performance in all three cases of parameter perturbations, step disturbance input and sensor noise to correlate the results.

Starting with the first case of parameter perturbations, two simulation sets were prepared. The first set is for mass (*m*) and moment of inertia (*J*) parameters and the second one is for the velocity (*v*) parameter. Perturbation amount was set to lie within ±%20 for these simulation sets. The first set of simulation results are shown in Fig. 16.

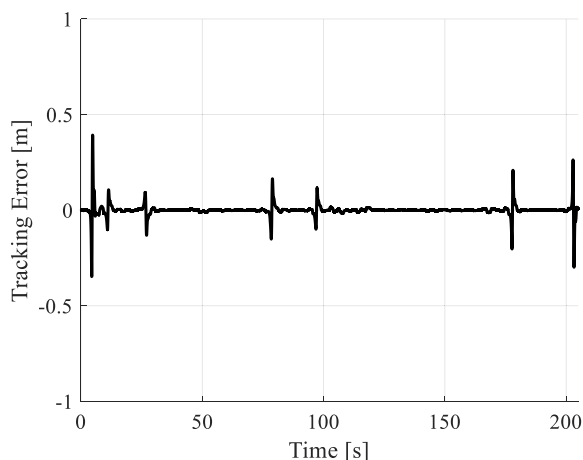


FIGURE 14. The automated path following vehicle’s path tracking error is shown here while following the path within the campus environment in Figure 13. The error values are very small showing that the parameter space designed multi-objective digital PD steering controller has performed satisfactorily.

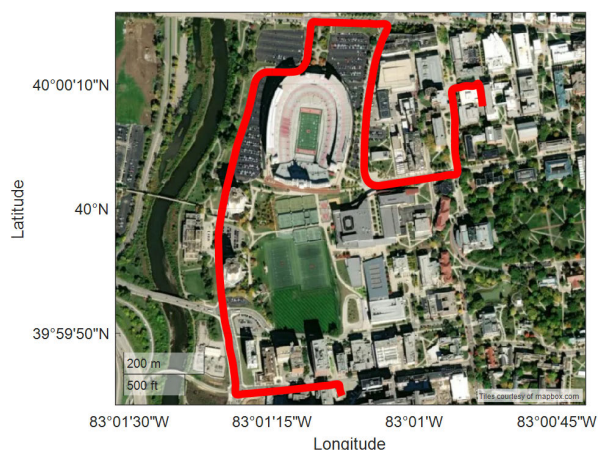


FIGURE 15. Simulated vehicle path in the OSU campus environment plotted on the satellite image.

Five different simulation results can be seen in Fig. 16 where the vehicle parameters change with each simulation. Results were colored according to their perturbation amount, which can also be seen at top right in the figure. As expected, with higher mass and moment of inertia, tracking error increases, but still stays in a reasonable range and the vehicle motion does not become unstable. When mass and moment of inertia are reduced in the path following simulations, error can be seen to be reduced significantly. The next simulation set investigates the performance in a similar manner with five different simulations, but in this case the variable parameter was chosen to be the velocity. Results can be seen in Fig. 17. It is important to note that a normalized time scale was used while showing these results in order to compare the results more easily. The normalized time scale was used, since with changing velocity, the time for the vehicle to complete the track changes, as well as the times for the curvature encounters and it would result in a very hard to read graph with no meaningful comparison capability if this were not done.

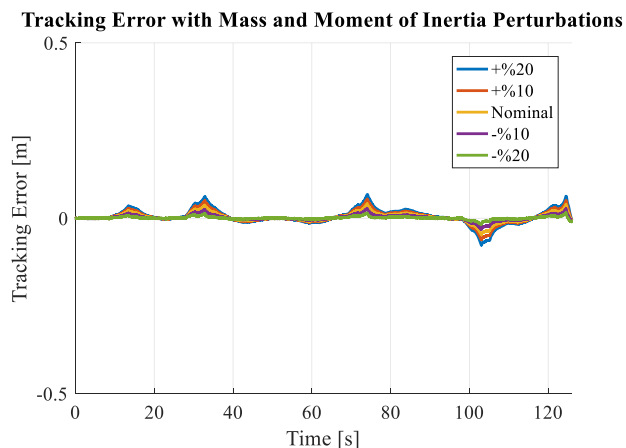


FIGURE 16. The automated path following vehicle’s path tracking error is shown here with mass and moment of inertia parameter perturbations, while following the race track path shown in Figure 11. Error values stay relatively small and the vehicle does not become unstable.

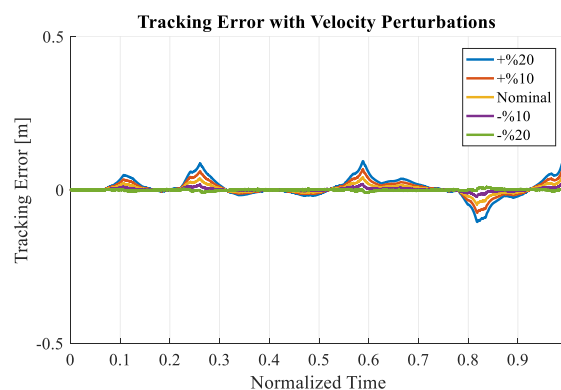


FIGURE 17. The automated path following vehicle’s path tracking error is shown here with velocity parameter perturbation, while following the race track path shown in Figure 11. Error values stay relatively small and the vehicle motion does not become unstable.

Similar to the previous case, five different simulation results were shown as color coded lines in Fig. 18. Again, as expected, tracking error increases with increase in the velocity parameter, but it is still reasonable, and the vehicle stays stable in all simulations.

For the second case, controller performance with disturbance was tested. While the vehicle is following the path in the real world, disturbances might be caused by various factors. One of the most common ones is the wind disturbance. Wind that comes from the side of the vehicle, applies a moment force on the vehicle, resulting a variation in yaw rate. This disturbance was implemented in the model, while keeping the effect as close as possible to a real world scenario. A heavy wind would suddenly hit the vehicle and cause an impulse effect on the yaw rate of the vehicle, while the vehicle is following the path. The model was modified to provide a yaw rate disturbance of π rad/s as an impulse ($timestep = 0.01s$) at 45s. Afterwards, another impulse was applied with opposite direction at 55s with 2 times the value. The effect of this disturbance was shown in Fig. 19 with zoomed time and value axes for better readability. Overall tracking error was

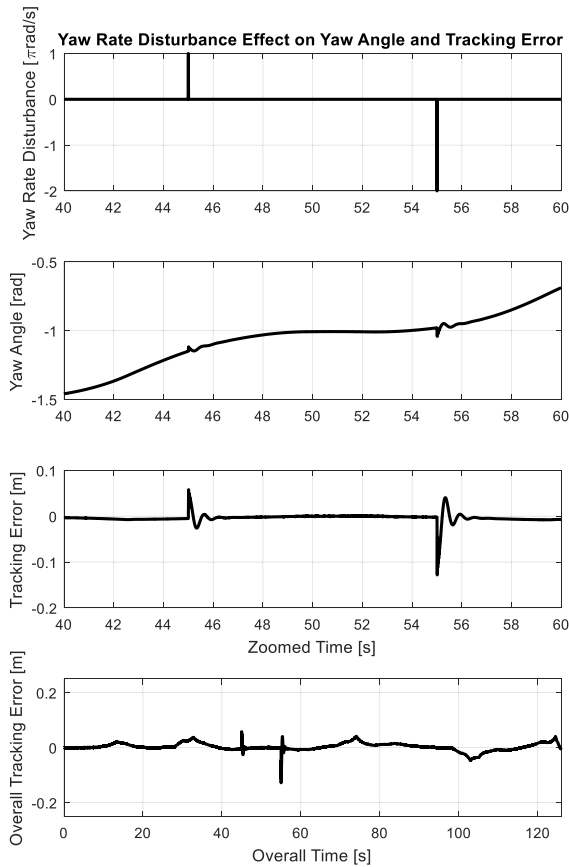


FIGURE 18. Yaw rate disturbance effect on vehicle yaw angle and tracking error is shown, while the vehicle is following the race track path shown in Figure 11. Error values stay relatively small and the vehicle motion does not become unstable.

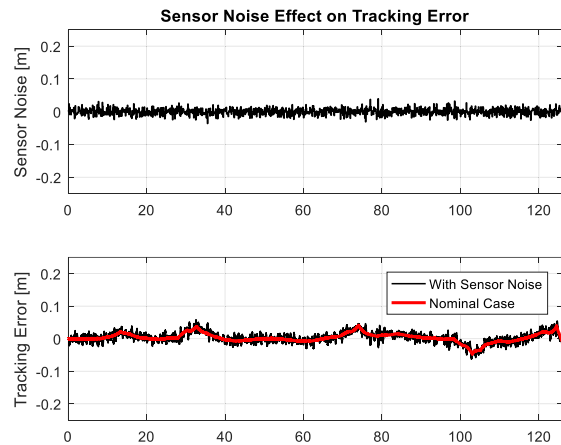


FIGURE 19. Sensor noise effect on tracking error is shown while the vehicle is following the race track path shown in Figure 11. Error values stay relatively small and the vehicle motion does not become unstable.

also shown with overall time to provide a larger picture of the simulation.

It can be seen in Fig. 18 that sudden disturbance caused by the wind on vehicle yaw rate result in a shift in vehicle yaw angle, which causes additional tracking error. The controller immediately responds to this effect and manages to bring the vehicle back to course in very short time with minimal

oscillation. More importantly, the vehicle motion does not become unstable.

For the third and final case, the effect of sensor noise was investigated. This effect was implemented as a noise on tracking error measurement, since it is the output of the closed loop system. Noise was implemented as a white noise with 0.1s sample time, which corresponds to 1/10th of simulation timestep. Results can be seen in Fig. 19.

Applied sensor noise can be seen within the plot on top in Fig. 19. In the bottom plot, two different tracking error results for two different simulations, with and without sensor noise applied, were plotted for comparison. Looking at the tracking error, it can be seen that the sensor noise does not have a large effect on the overall behavior of the tracking error other than adding noise on top of it. The error still stays in reasonable range and the vehicle does not become unstable.

Under this subsection, controller performance was tested against parameter perturbations, disturbance input and sensor noise injection. Looking at the overall results, it can be seen that the controller performs well in terms of stability and robustness in all three cases.

V. CONCLUSION

This paper introduced a parameter space approach based multi-objective digital PID controller design method. Absolute stability, phase margin constraint, gain margin constraint and mixed sensitivity constraint were treated as the multiple objectives. In an illustrative example, multi-objective robust digital PD controller gains were designed considering phase margin constraint and mixed sensitivity constraint simultaneously and used in the feedback control system of autonomous vehicle path following. Simulation results using different types of paths, as well as the evaluation of the controller under parameter perturbations, disturbance and sensor noise effects, show the effectiveness of the proposed digital controller design method. The approach used in this paper can be extended to design robust parameter space based disturbance observer control [3], [24]. The multi-objective digital PID controller design method of this paper can also be applied to different application areas in future work [25], [26].

REFERENCES

- [1] S. P. Bhattacharyya, H. Chapellat, and L. H. Keel, *Robust Control: The Parametric Approach*. Englewood Cliffs, NJ, USA: Prentice-Hall, 1995.
- [2] J. Ackermann, P. Blue, T. Bunte, L. Guvenc, D. Kaesbauer, M. Kordt, M. Muhler, and D. Odenthal, *Robust Control: The Parameter Space Approach*. London, U.K.: Springer-Verlag, 2002.
- [3] L. Guvenc, B. A. Guvenc, B. Demirel, and M. T. Emirler, *Control of Mechatronic Systems*. London, U.K.: IET, 2017.
- [4] B. Demirel and L. Güvenç, “Parameter space design of repetitive controllers for satisfying a robust performance requirement,” *IEEE Trans. Autom. Control*, vol. 55, no. 8, pp. 1893–1899, Aug. 2010.
- [5] L. Güvenç and J. Ackermann, “Links between the parameter space and frequency domain methods of robust control,” *Int. J. Robust Nonlinear Control*, vol. 11, no. 15, pp. 1435–1453, Dec. 2001.
- [6] S. Oncu, S. Karaman, L. Guvenc, S. S. Ersolmaz, E. S. Ozturk, N. Kilic, and M. Sinal, “Steer-by-wire control of a light commercial vehicle using a hardware-in-the-loop test setup,” in *Proc. IEEE Intell. Vehicles Symp.*, vol. 15, Jun. 2007, pp. 852–859.

- [7] B. A. Guvenc and L. Guvenc, "Robust steer-by-wire control based on the model regulator," in *Proc. Int. Conf. Control Appl.*, Glasgow, U.K., 2002, pp. 435–440.
- [8] M. T. Emirler, İ. M. C. Uygan, B. A. Güvenç, and L. Güvenç, "Robust PID steering control in parameter space for highly automated driving," *Int. J. Veh. Technol.*, vol. 2014, Feb. 2014, Art. no. 259465.
- [9] S. Necipoglu, S. A. Cebeci, Y. E. Has, L. Guvenc, and C. Basdogan, "Robust repetitive controller for fast AFM imaging," *IEEE Trans. Nanotechnol.*, vol. 10, no. 5, pp. 1074–1082, Sep. 2011.
- [10] B. Orun, S. Necipoglu, C. Basdogan, and L. Guvenc, "State feedback control for adjusting the dynamic behavior of a piezoactuated bimorph atomic force microscopy probe," *Rev. Sci. Instrum.*, vol. 80, no. 6, 2009, Art. no. 063701.
- [11] J. Ackermann and D. Kaesbauer, "Stable polyhedra in parameter space," *Automatica*, vol. 39, no. 5, pp. 937–943, May 2003.
- [12] M. T. Söylemez, N. Munro, and H. Baki, "Fast calculation of stabilizing PID controllers," *Automatica*, vol. 39, no. 1, pp. 121–126, Jan. 2003.
- [13] M. Saeki, "Properties of stabilizing PID gain set in parameter space," *IEEE Trans. Autom. Control*, vol. 52, no. 9, pp. 1710–1715, Sep. 2007.
- [14] K. J. Åström and T. Hägglund, "Revisiting the Ziegler–Nichols step response method for PID control," *J. Process Control*, vol. 14, no. 6, pp. 635–650, Sep. 2004.
- [15] S. Skogestad, "Simple analytic rules for model reduction and PID controller tuning," *J. Process Control*, vol. 13, no. 4, pp. 291–309, Jun. 2003.
- [16] U. M. Nath, C. Dey, and R. K. Mudi, "Desired characteristic equation based PID controller tuning for lag-dominating processes with real-time realization on level control system," *IEEE Control Syst. Lett.*, vol. 5, no. 4, pp. 1255–1260, Oct. 2021.
- [17] R. Farkh, M. Ksouri, and F. Bouani, "Optimal robust control for unstable delay system," *Comput. Syst. Sci. Eng.*, vol. 36, no. 2, pp. 307–321, 2021.
- [18] H. Habibi, H. R. Nohooji, and I. Howard, "Adaptive PID control of wind turbines for power regulation with unknown control direction and actuator faults," *IEEE Access*, vol. 6, pp. 37464–37479, 2018.
- [19] J.-W. Perng and S.-C. Hsieh, "Design of digital PID control systems based on sensitivity analysis and genetic algorithms," *Int. J. Control, Autom. Syst.*, vol. 17, no. 7, pp. 1838–1846, Jul. 2019.
- [20] Z. Qi, Q. Shi, and H. Zhang, "Tuning of digital PID controllers using particle swarm optimization algorithm for a CAN-based DC motor subject to stochastic delays," *IEEE Trans. Ind. Electron.*, vol. 67, no. 7, pp. 5637–5646, Jul. 2020.
- [21] I. D. Diaz-Rodriguez, V. A. Oliveira, and S. P. Bhattacharyya, "Modern design of classical controllers: Digital PID controllers," in *Proc. IEEE 24th Int. Symp. Ind. Electron. (ISIE)*, Buzios, Brazil, Jun. 2015, pp. 1010–1015.
- [22] S. Li, C. K. Ahn, and Z. Xiang, "Sampled-data adaptive output feedback fuzzy stabilization for switched nonlinear systems with asynchronous switching," *IEEE Trans. Fuzzy Syst.*, vol. 27, no. 1, pp. 200–205, Jan. 2019, doi: 10.1109/TFUZZ.2018.2881660.
- [23] H. Wang, A. Tota, B. Aksun-Guvenc, and L. Guvenc, "Real time implementation of socially acceptable collision avoidance of a low speed autonomous shuttle using the elastic band method," *Mechatronics*, vol. 50, pp. 341–355, Apr. 2018.
- [24] L. Güvenç and K. Srinivasan, "Force controller design and evaluation for robot-assisted die and mould polishing," *Mech. Syst. Signal Process.*, vol. 9, no. 1, pp. 31–49, Jan. 1995.
- [25] M. T. Emirler, K. Kahraman, M. Senturk, B. Aksun-Guvenc, L. Guvenc, and B. Efendioglu, "Lateral stability control of fully electric vehicles," *Int. J. Automot. Technol.*, vol. 16, no. 2, pp. 317–328, 2015.
- [26] A. Boyali and L. Guvenc, "Real-time controller design for a parallel hybrid electric vehicle using neuro-dynamic programming method," *IEEE Int. Conf. Syst., Man Cybern.*, Istanbul, Turkey, Oct. 2010, pp. 4318–4324.



interests include steering control and path following control of autonomous vehicles and parameter space based robust control.



Okan University. From 2015 to 2016, he was a Researcher with Istanbul Technical University for a project which was financially supported by the Scientific and Technological Research Council of Turkey. Since 2017, he has been a Graduate Research Associate with The Ohio State University. His research interests include software and hardware implementation for autonomous driving, HIL simulations, collision avoidance, and V2X communication.



He is a member of the International Federation of Automatic Control (IFAC) Technical Committees on Automotive Control, Mechatronics, and Intelligent Autonomous Vehicles and the IEEE Technical Committees on Automotive Control, and Intelligent Vehicular Systems and Control. He was the General Chair of the 2007 IEEE Intelligent Vehicles Symposium. He was the Co-Ordinator of Team Mekar in the 2011 Grand Cooperative Driving Challenge. He is an ASME Fellow. His work on connected and autonomous driving has resulted in nine research prototype vehicles (two of them with a major automotive OEM) with different levels of autonomy, the last four being with the Automated Driving Laboratory, The Ohio State University. He was a member of the Connected Vehicle Environment and Autonomous Vehicle working groups of the City of Columbus Smart City Challenge project.

• • •